Research Article

Microstructure and properties of porous Si3N4 ceramics by gelcasting–self-propagating high-temperature synthesis (SHS)

Shile CHEN[a], Liang WANG[b], Gang HE[b], Jiangtao LI[b,*], Chang-An WANG[a,*]

[a]*State Key Laboratory of New Ceramics and Fine Processing, School of Materials Science and Engineering, Tsinghua University, Beijing 100084, China*
[b]*CAS Key Laboratory of Cryogenics, Technical Institute of Physics and Chemistry, Chinese Academy of Sciences, Beijing 100190, China*

Abstract: Porous silicon nitride ceramics have attracted a considerable attention due to their excellent overall performance, but poor porosity homogeneity and structural shrinkage induced by prolonged high temperature sintering limit its further application. Herein, as a three-in-one solution for the above issues, for the first time we develop a novel approach that integrates the merits of gelcasting–SHS (self-propagating high-temperature synthesis) to prepare porous Si_3N_4 ceramics to simultaneously achieve high porosity, high strength, high toughness, and low thermal conductivity across a wide temperature range. By regulating the solid content, porous Si_3N_4 ceramics with homogeneous pore structure are obtained, where the pore size falls inbetween 1.61 and 4.41 μm, and the elongated grains are interlaced and interlocked to form micron-sized coherent interconnected pores. At the same time, porous Si_3N_4 ceramics with porosity of 67.83% to 78.03% are obtained, where the compressive strength reaches 11.79 to 47.75 MPa and fracture toughness reaches 1.20 to 6.71 MPa·m$^{1/2}$.

Keywords: porous Si_3N_4 ceramics; gelcasting; self-propagating high-temperature synthesis (SHS); porosity

1 Introduction

Si_3N_4 ceramics boasting superior mechanical properties, thermal stability, chemical stability, and oxidation resistance, are among the best materials for structural ceramics in terms of integrated performance [1–3]. Surprisingly, when pores (an air phase) are incorporated into the structure, their functionalities are extended significantly. Porous Si_3N_4 ceramics have the characteristics of low density, low thermal conductivity, and low dielectric loss, which in turn impart light weight, thermal insulation, and wave-transparent properties [4–6]. Consequently, in order to achieve high-performance porous Si_3N_4 ceramics, i.e., both porosity and strength, the following research interests have gained considerable popularity: (a) As the most essential microstructure of porous ceramics, the methods of constructing pore structure are constantly innovated, 3D printing [7], pore former [8,9], freeze-drying [10–12], gelcasting [8,13], and hollow Si_3N_4 microsphere [14] methods, etc.; (b) breakthroughs in the synthesis technique of porous Si_3N_4, SHS (self-propagating high-temperature synthesis) [15–18], chemical vapor deposition [19], and carbothermal reduction nitridation

[20] enrich the range of methods. It is undeniable that these efforts have broadened the application fields of porous Si_3N_4 ceramics. Nonetheless, nearly all of them have achieved at the expense of their simplicity and porosity–strength. For example, SHS allows for fast and simple synthesis of porous Si_3N_4 with low porosity, and chemical vapor deposition method provides porous Si_3N_4 with high porosity and excellent mechanical properties in a cumbersome process. In the research of porous Si_3N_4 ceramics by self-propagating synthesis, many process factors, such as N_2 pressure [17], reactant composition [16], and sintering aid [18], have been systematically studied. However, the effect of forming technology on the morphology and properties of porous Si_3N_4 ceramics has been neglected in the existing studies, and the porosity of porous Si_3N_4 ceramics is generally low. Although the porous Si_3N_4 ceramics prepared by the pore-former–SHS method [9] have high porosity, the homogeneity of the porous structure is difficult to be guaranteed.

The microstructure of porous ceramics determines their properties, and the optimization of the properties can be realized by modulating the structure. Based on our previous research [21–23], gelcasting process using tert-butyl alcohol (TBA) as the medium can enable porous ceramics with homogeneous and dimensionally adjustable pore structure, which has obvious advantages over the pore former and foaming methods.

In addition, the strong Si–N covalent bond and high grain boundary energy of Si_3N_4 lead to its low sintering driving force. Sintering at high temperatures for long time not only consumes a lot of energy but also tends to cause structural shrinkage of porous ceramics. In sum, the preparation of high-quality porous Si_3N_4 ceramics is not an easy task. Herein, we have integrated the advantages of the gelcasting–SHS process for the first time to achieve porous Si_3N_4 ceramic structure with high porosity and high toughness. At the same time, the structure of porous Si_3N_4 ceramics has been systematically investigated, including grain aspect ratio and pore structure, etc. It offered a new perspective to obtain porous ceramics with high porosity and high performance easily and quickly.

2　Experimental

2.1　Preparation of porous green body by gelcasting

The Si_3N_4 powder ($d_{50} \approx 10$ μm, α-Si_3N_4 > 93%, self-made by combustion synthesis) as well as Si powder (> 99.99 %, $d_{50} \approx 3$ μm; Sinopharm Chemical Reagent Co., Ltd., Beijing, China) were used as raw materials, and Y_2O_3 powder ($d_{50} \approx 50$ nm, 99.9% purity; Sinopharm Chemical Reagent Co., Ltd., Beijing, China) was used as the sintering aid. Acrylamide (AM, $C_2H_3CONH_2$, Merck, USA), N,N'-methylene bisacrylamide (MBAM, $(C_2H_3CONH_2)_2CH_2$, Merck, USA), TBA ($C_4H_{10}O$; Aladdin, China), ammonium persulfate (APS, $(NH_4)_2S_2O_8$, Merck, USA), and N,N,N',N'-tetramethylethylenediamine (TEMED, $C_6H_{16}N_2$, Merck, USA) were used as the monomers, crosslinker, solvent, initiator, and catalyst in the gelcasting process, respectively. A powder mixture of 60 wt% Si_3N_4, 40 wt% Si, and Y_2O_3 powder (which accounts for 4.7 wt% of the total weight of Si_3N_4 and Si powder) were dispersed throughout the premix solution of monomers to enable the slurry to reach the corresponding solid contents (10, 15, 20, and 25 vol%). The premix solution was obtained by dissolving 14.5 wt% (based on premix solution) of monomer and 0.5 wt% (based on premix solution) of crosslinker in TBA. The slurry was ground for 30 min with the vibrating ball milling. The composition of gelcasting slurry with different solid contents were listed in Table 1. And then the obtained slurry was vacuum degassed for 10 min. Finally, a certain amount of catalyst and initiator is added to the slurry successively and mixed well, then poured into the mold, and transferred to the oven for curing and drying.

2.2　Synthesis of porous Si_3N_4 ceramics via the self-propagation process

According to the thermogravimetric (TG) curve of the green body (Fig. S1(a) in the Electronic Supplementary Material (ESM)), the dried green bodies were heated in Ar using the heating curve in Fig. S1(b) in the ESM to remove the organics. Afterward, the obtained green bodies were immersed into a powder bed which is composed of Si and β-Si_3N_4 powder in the mass ratio of 1:1, and the pellet is ignited by combustion of the powder bed. The rectangular shaped porous graphite

Table 1　Initial composition of gelcasting slurry with different solid contents

Solid content (vol%)	Si (wt%)	Si_3N_4 (wt%)	Y_2O_3[a] (wt%)	Premix solution[b] (mL)
10	40	60	4.7	45
15	40	60	4.7	42.5
20	40	60	4.7	40
25	40	60	4.7	37.5

[a]Based on weight of Si_3N_4 and Si; [b]the mass proportion of premix solution: 85 wt% TBA, 14.5 wt% monomer, and 0.5 wt% crosslinker.

mold with powder bed and green bodies were placed in a high-pressure reactor and filled with high-purity nitrogen of 4 MPa. The tungsten wire coil at one end of the mold is electrified and heated to ignite a small amount of Ti powder ignition agent around the coil to initiate the combustion synthesis reaction of Si and N_2. The W–Re thermocouple inserted into the green bodies was used to detect the temperature change during combustion reaction.

2. 3   Characterization

The morphology and microstructure of the samples were investigated by an S-4800 scanning electron microscope (SEM; Zeiss Merin Compalt, Germany) equipped with the energy-dispersive X-ray spectroscopy (EDS; Oxford Instruments X-MaxN, UK). The phase composition of the samples was collected by Bruker D8-Advance diffractometer employing Ni-filtered Cu Kα radiation (λ = 0.154 nm) with 40 kV of working voltage. Thermogravimetric analysis (TGA) curve of the sample was measured by a TA Q5000IR thermal analyzer under Ar. The Archimedes' method was used to measure bulk density and porosity of porous Si_3N_4 ceramics, and the pore size distributions were determined by mercury intrusion porosimeter. The chemical state and the bonding state of porous Si_3N_4 ceramics were obtained by the X-ray photoelectron spectroscopy (XPS; Thermo Scientific ESCALAB 250Xi, UK). Heat capacity of porous Si_3N_4 ceramics was characterized using a physical property measurement system (PPMS; 9T QD, Quantum Design, San Diego, CA, USA) at 25 ℃. The thermal diffusion coefficient of the porous Si_3N_4 ceramics was measured by using a laser thermal conductivity meter (NETZSCH, LFA467, USA). The compressive strength was measured by a mechanical testing machine (AG-2000A, Shimadzu, Kyoto, Japan) with dimensions of 5 mm × 5 mm × 5 mm and a cross-head speed of 0.5 mm/min. The flexural strength of the sample was tested by the method of three-point bending (AG-IC20KN, SHIMADZU, Japan), the sample size is 1.5 mm × 2 mm × 25 mm, the span of this test is 20 mm, and the loading rate is selected as 0.2 mm/min. The fracture toughness of porous Si_3N_4 ceramics was loaded in the same way as the three-point bending test, and the test specimen size is 4 mm × 2 mm × 20 mm with a notch width of less than 0.2 mm, the span of this test is 16 mm, and the loading rate is selected 0.05 mm/min. All the mechanical properties were obtained by testing five samples and taking the average.

3   Results and discussion

The phase composition and morphology of the gelcasting green body before SHS are shown in Fig. 1. The green body is composed of various phases: the main crystalline phase is the Si as the reaction raw material, both α and β crystalline phases of Si_3N_4 used as a diluent are existed, and a weak Y_2O_3 diffraction peak is also found. Gelcasting relies on the *in-situ* polymerization of acrylamide to form a three-dimensional spatial network structure [21], allowing the preparation of the green body with a loose and uniform interconnected pore structure, and homogeneous dispersion of the original powder within the green body, as shown in Fig. 1(b). In addition, the green body has considerable mechanical strength (Fig. S2 in the ESM). As shown in Fig. 2(a), the pore size of the gelcasting green body decreases with the increase of the solid content, and the pore size is about 1.12–3.98 μm. Meanwhile, the porosity reaches the maximum when the solid content is 15 vol%. The shrinkage of low solid content is greater during drying and debinding, which leads to the porosity of 10 vol% solid content is lower than that of 15 vol% solid content.
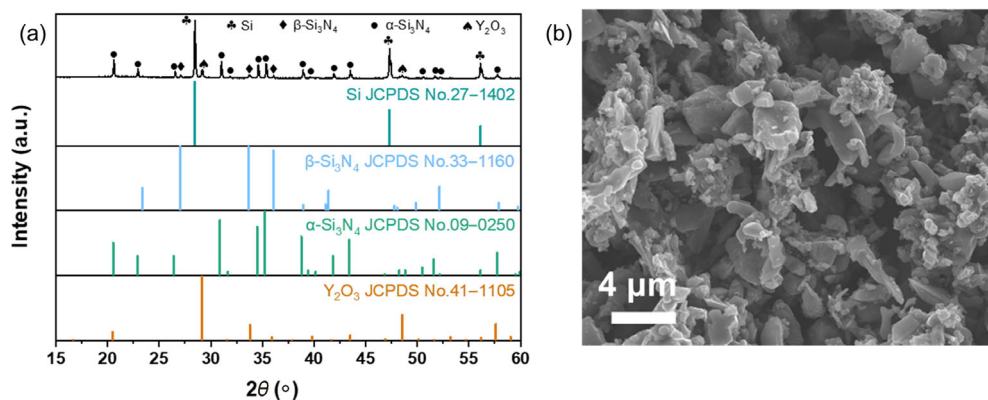

Fig. 1   (a) XRD patterns and (b) SEM image of the green body with 20 vol% solid content.
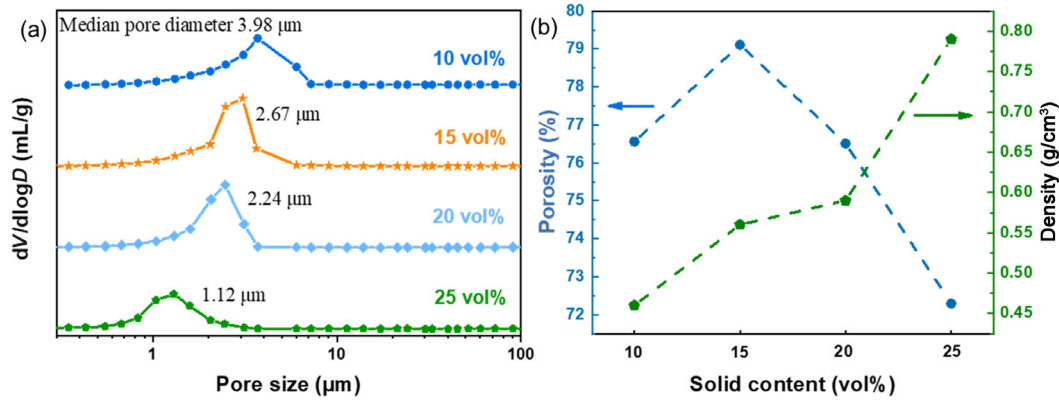
Fig. 2 (a) Pore size distributions of the gelcasting green bodies with variable solid contents and (b) density and porosity of the gelcasting green bodies.

It can be seen from the temperature monitoring in the process of self-propagating reaction (as shown in Fig. 3) that the solid content affects the reaction temperature and time (detailed parameters are shown in Table 2). With the increase of the solid content, heating rate, maximum temperature, and reaction time all increase accordingly. The dark brown, smooth, and crack-free surface of the green body, as shown in Fig. 4(a), was transformed into grayish-white porous Si_3N_4 ceramics after SHS. The porosity and density of porous Si_3N_4 ceramics with a variety of solid contents are shown in Fig. 4(b). In sum, the porosity rises from 67.83% to 78.03% with the solid content, and the density of the porous Si_3N_4 ceramics decreases simultaneously, reaching a minimum (0.71 g/cm^3) when the solid content is 10 vol%. Figure 4(c) illustrates the linear shrinkage of porous Si_3N_4 ceramics after SHS. It is noteworthy that the linear shrinkage increases significantly at 10 vol% solid content, and the considerable shrinkage performance will change the porosity. Despite the fact that SHS completes both nitriding and sintering processes in a remarkably short period of time [24–26], the internal particle build-up of a low solid content (10 vol%) is so loose that dramatic sintering shrinkage occurs when the combustion wave passes through. It explains the increase in porosity when the solid content is increased from 10 to 15 vol%, which is consistent with the trend of porosity change in the green body. Obviously, high solid content significantly reduces linear shrinkage in the SHS.

The pore size distributions of the porous Si_3N_4 ceramics are investigated in Fig. 5. The peaks of the pore size distribution curves gradually shift to the left when the solid content increases from 10 to 25 vol%, indicating a gradual reduction in pore size from 4.41 to
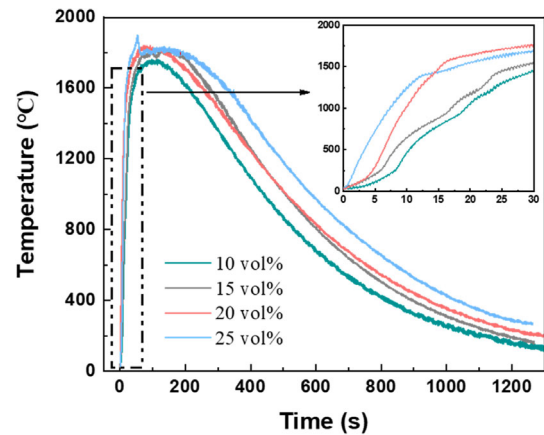

**Fig. 3** Temperature curves of green bodies during the SHS process.

Table 2 Combustion temperature, reaction time, and porosity and density of green bodies obtained with different solid contents

Solid content (vol%)	Porosity (%)	Density (g/cm^3)	N_2 pressure (MPa)	T_{max} (℃)	Reaction time (s)
10	76.56	0.46	4	1756	255
15	79.11	0.56	4	1822	321
20	76.51	0.59	4	1838	324
25	72.29	0.79	4	1900	390

1.61 µm. In addition, the sharp single peaks also imply that the porous Si_3N_4 ceramics have a homogeneous pore structure. The key lies in the fact that the gelcasting green body has high porosity and uniformly connected porosity structure, and SHS technology can greatly shorten the sintering time and reduce the sintering shrinkage, so that the structural advantage can be retained. Compared to the reported porous Si_3N_4 ceramics [9], the gelcasting–SHS allows for preparation of well-structured porous Si_3N_4 ceramics with small pore size and homogeneous pore size distribution without the assist
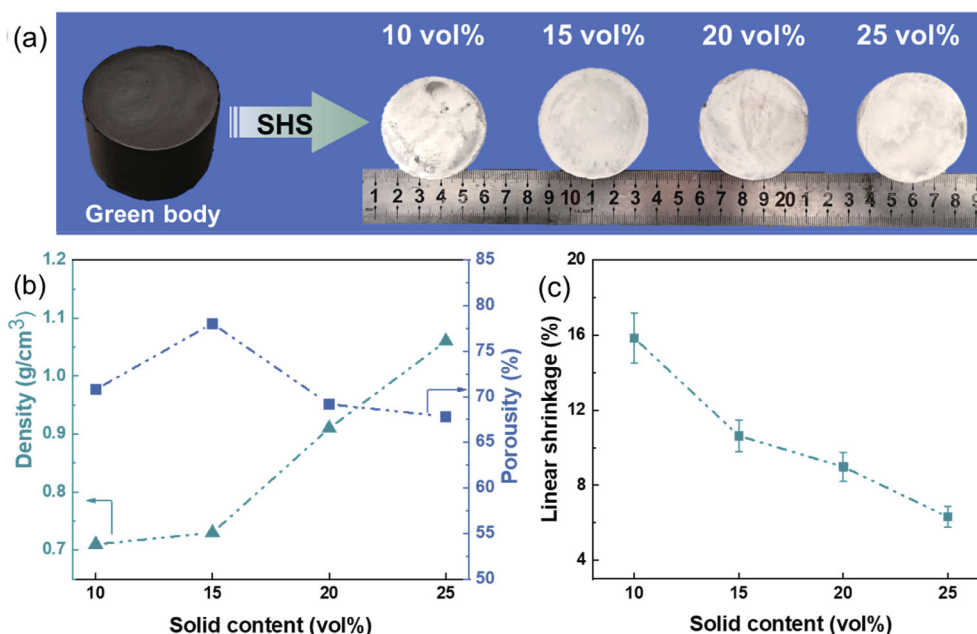
Fig. 4 (a) Digital photos of the green body with gelcasting and porous Si_3N_4 ceramics with different solid contents after SHS, (b) density and porosity of porous Si_3N_4 ceramics synthesized by self-propagation, and (c) linear shrinkage of porous Si_3N_4 ceramics with various solid contents.
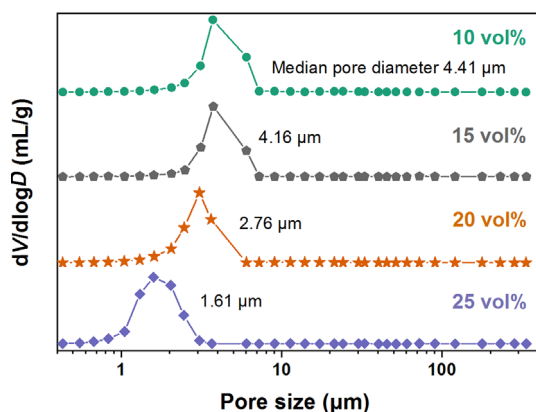

Fig. 5 Pore size distributions of porous Si_3N_4 ceramics with variable solid contents.

of pore forming agents. Hence the integration of the superiority of gelcasting and SHS enables the production of porous Si_3N_4 with high porosity, low density, and uniformly interconnected pores.

The phase composition of the porous Si_3N_4 ceramics with different solid contents was analyzed by XRD, and the results are shown in Fig. 6. Figure 6(a) illustrates the XRD patterns of cross-sections of porous Si_3N_4 ceramics. Almost all the diffraction peaks of the samples can be well indexed to the β-phase of Si_3N_4 (JCPDS No. 33-1160) with different solid contents. A sufficiently high temperature combustion wave passes through the green body, the Si is vaporized and nitrided, while simultaneously the α-phase Si_3N_4 is completely transformed

into the β-phase through the dissolution precipitation process [15]. In another aspect, the high porosity speeds up the reaction between Si and N_2, which augments the phase transition process [9,15]. It is also observed that a weak diffraction peak of SiC (JCPDS No. 29-1129) appears near the diffraction angle of 36° in the XRD pattern. The intensity of the SiC diffraction peak gradually decreases with increasing solid phase content, which is attributed to the decrease of acrylamide in premix solution. The TG curve in Fig. 6(b) corroborates that the carbon source for the SiC is mainly from the acrylamide in the premix solution, which also retains about 4 wt% carbon at 1000 ℃. Nevertheless, the XRD patterns of the porous Si_3N_4 ceramics' surface (in Fig. 7) revealed no characteristic peak of SiC phases other than β-Si_3N_4, which may be associated with the fact that organics and residual carbon at the surface tend to escape at high temperatures. But besides SiC diffraction peaks, a broad peak of residual amorphous carbon appears in the porous Si_3N_4 ceramics without binder removal treatment, as shown in Fig. S3 in the ESM.

The morphology of the porous Si_3N_4 ceramics prepared by SHS is presented in Fig. 8. Overall, the long rod-like grains are interlaced and interlocked to form micron-sized coherent interconnected pores, which is consistent with the results of the pore size distribution. The low-temperature eutectic phase formed by Y_2O_3 with SiO_2 on the surface of Si_3N_4 accelerates the atomic diffusion rate and boosts
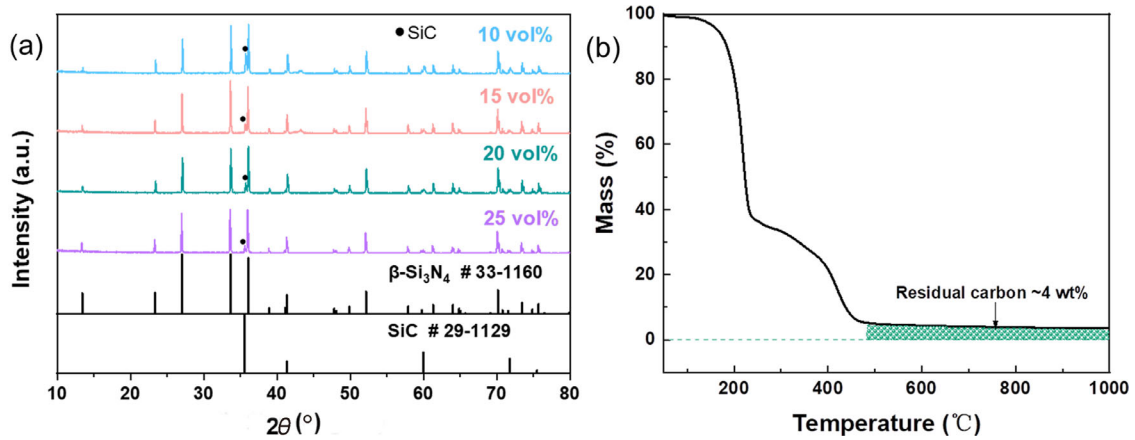
Fig. 6 (a) XRD patterns of cross-sections of porous Si_3N_4 ceramics with different solid contents and (b) TG curve of polyacrylamide in Ar.
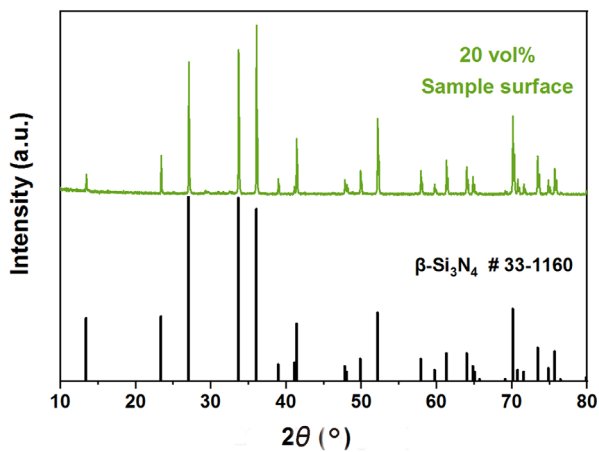
Fig. 7 XRD patterns of surface of porous Si_3N_4 ceramics with 20 vol% solid content.

the development of elongated rod-like grains [15–17]. More importantly, the formation mechanism of Si_3N_4 obtained by SHS is controlled by vapor–crystal (VC) mechanism [24–26]. The rapid increase in temperature (far beyond Si melting point) gives rise to a fast vaporization rate of Si and further react with N_2, leading to the formation and growth of Si_3N_4 on the surface of the both Si particles and Si_3N_4 particles. The loose and porous internal space of the gelcasting green body facilitates favorable conditions for sufficient N_2 contact and the growth of long rod-like grains of β-Si_3N_4 during SHS. The grains' average length, average width, and average aspect ratio are statistically presented in Table 3. The obtained porous Si_3N_4 ceramics are
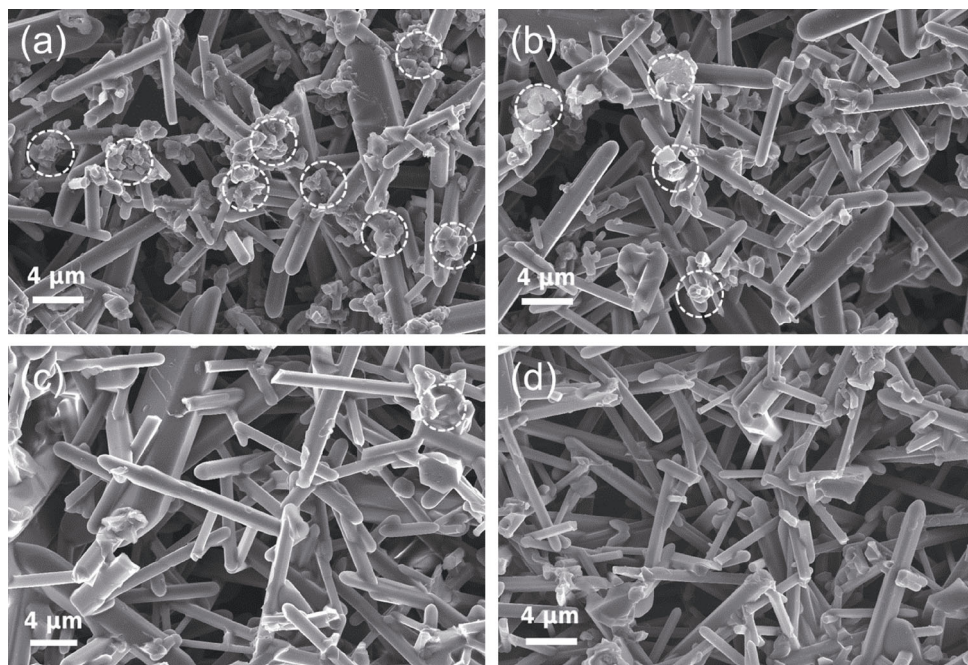
Fig. 8 Fractography of porous Si_3N_4 ceramics with different solid contents: (a) 10 vol%, (b) 15 vol%, (c) 20 vol%, and (d) 25 vol%.

Table 3   Average grain size of porous Si₃N₄ ceramics obtained with different solid contents

Solid content (vol%)	10	15	20	25
Average length (μm)	17.4±3.89	13.642±3.13	10.25±2.66	7.75±1.05
Average width (μm)	1.84±0.6	1.624±0.63	1.07±0.27	0.93±0.09
Average aspect ratio	10.07±2.34	9.66±1.39	8.99±1.91	8.34±0.79

distinguished by their long grain length and high aspect ratio, which are further enhanced by the reduction in the solid content. As a consequence, elongated single intact grains with high aspect ratio can be easily observed, which is completely distinct from the porous Si₃N₄ ceramic morphology prepared by dry compress–SHS [17].

In addition, a small amount of granular SiC with a uniform distribution is observed (circled in white in Fig. 8). It is noticeable that the increase in solid content assists in reducing the formation of SiC, intuitively verifying the XRD results. It is noteworthy that the SiC is mainly distributed in the interlaps of the β-Si₃N₄ grains (see Fig. S4 in the ESM), which seems to contribute to the mechanical strength of the porous ceramics.

To further analyze the elemental composition, chemical state, and electronic state of elements for the samples, XPS analysis was carried out on the porous Si₃N₄ ceramics. The XPS spectra of the porous Si₃N₄ ceramics are shown in Fig. 9. It is demonstrated that both of surface and cross-sections of porous Si₃N₄ ceramics only contain C, O, Si, Y, and N, no characteristic peak of other elements. High resolution XPS spectra of Si 2p taking from the surface position, only have one peak at binding energy of 102 eV representing Si₃N₄ [20,27], as shown in Fig. 9(b). In comparison, the Si 2p XPS spectrum is split into two single-peaks corresponding to SiC (103.6 eV) and Si₃N₄ (102 eV) existed in the

sample from cross-section [20,27–29]. Meanwhile, comparison of cross-section and surface of the EDS spectra in Fig. 10, intuitively confirms the presence of SiC at the grain intersection. The sample photo in Fig. S5 in the ESM observes that there is a color discrepancy between the surface and cross-section of the sample due to the presence of the SiC.

Thermal conductivity is one of the most important properties for porous ceramics considering the usage as thermal insulators. Herein, the heat transfer of porous Si₃N₄ ceramics has been investigated, as shown in Fig. 11. Its thermal diffusivity was measured using the laser-flash method in Fig. 11(a). The thermal diffusion coefficients of porous Si₃N₄ ceramics with various solid contents decrease gradually depending on the temperature. At the same time, the reduction in solid content causes a diminution in the heat conduction path, which contributes to the decrease in the thermal diffusion coefficient. The thermal conductivity (λ) was calculated with the following equation [30]:

$$\lambda = C_p \times \alpha \times \rho \tag{1}$$

where C_p is the specific heat capacity of porous Si₃N₄ ceramics obtained from physical property measurement system, α is the thermal diffusivity, and ρ is the density of the porous Si₃N₄ ceramics with various solid contents. Note that the slight decrease in the density due to thermal expansion is neglected, and the results are depicted in Fig. 11(b). The thermal conductivity of porous Si₃N₄ ceramics decreases gradually with increasing temperature up to 600 ℃, and then increases slowly with further increasing temperatures. The non-monotonic temperature dependence of the thermal conductivity is the result of a combination of three mechanisms [30]: (a) solid thermal conductivity, (b) gas thermal conductivity,
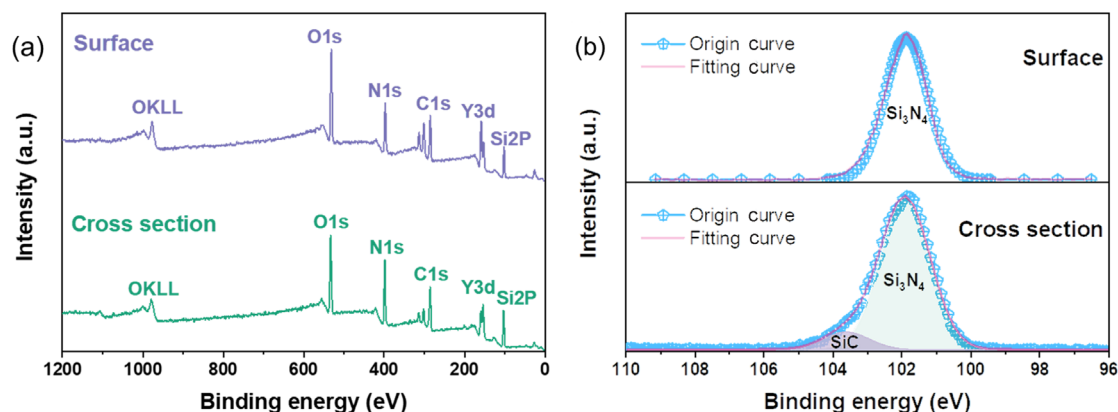
Fig. 9   (a) XPS spectra of porous Si₃N₄ ceramics with 20 vol% solid content and (b) high resolution XPS spectra of Si 2p for the porous Si₃N₄ ceramics with 20 vol% solid content.
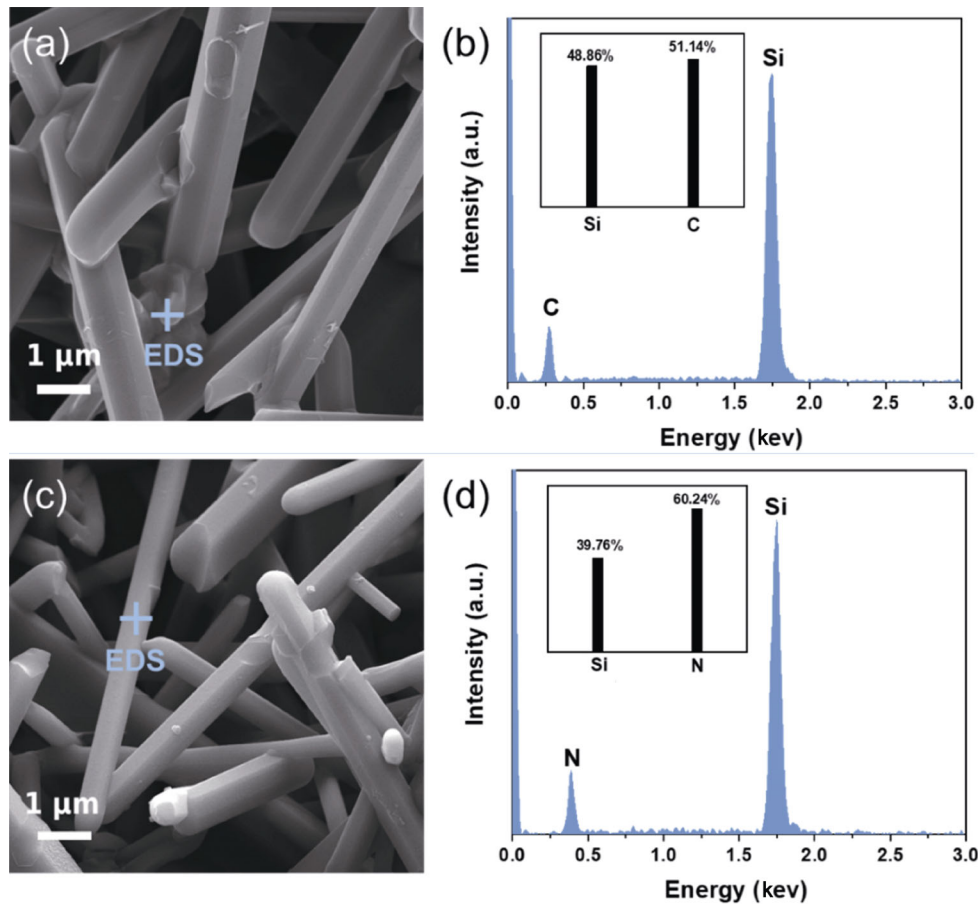
Fig. 10   EDS spectra of cross-section (a, b) and surface (c, d) of porous Si_3N_4 ceramics with 20 vol% solid content.
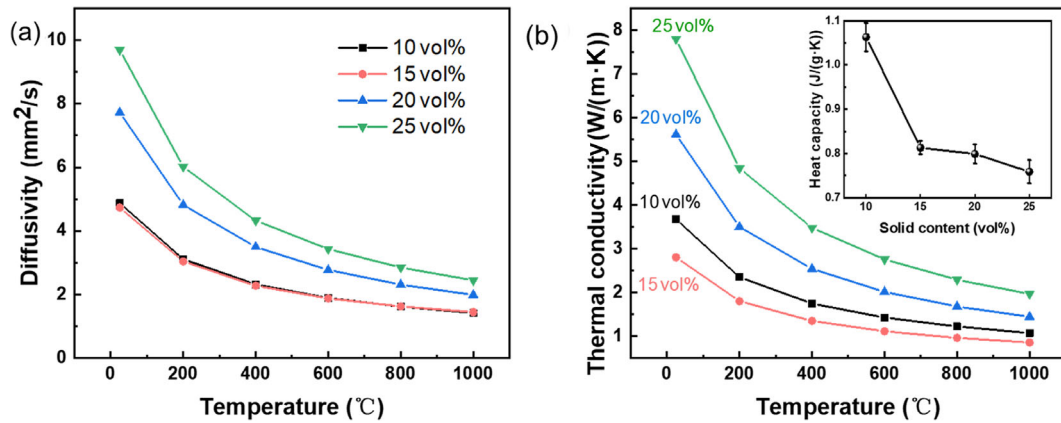

Fig. 11   (a) Temperature-dependent thermal diffusion coefficient of porous Si_3N_4 ceramics with different solid contents; (b) thermal conductivity of porous Si_3N_4 ceramics at various temperatures. The inset in (b) shows the specific heat capacity of samples with different solid contents.

and (c) radiative thermal conductivity. In particular, the thermal conductivity of the porous Si_3N_4 ceramics with 10 vol% solid content is higher than that of the 15 vol% sample, which is driven by the discrepancy in porosity. In general, porous ceramics have a low thermal conductivity, especially at high temperatures (minimum ≈ 1 W/(m·K)).

Mechanical properties are one of the most critical indicators of Si_3N_4 porous ceramics, and are governed by a combination of porosity, pore size, and morphology. The fracture toughness and flexural strength of the samples are exhibited in Fig. 12(a). The flexural strength of the samples does not rise linearly as the solid content increases, with the lowest strength (27 MPa) at 15 vol%
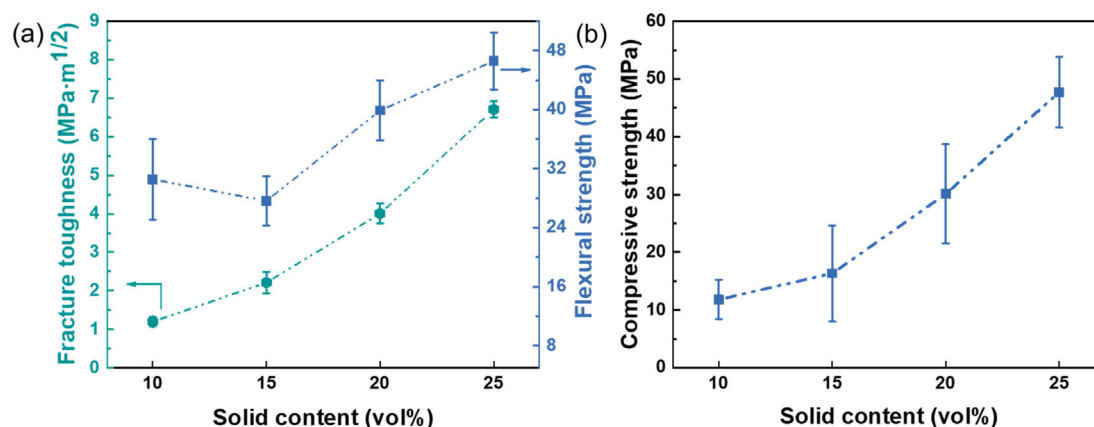
Fig. 12 Dependence of solid content on fracture toughness and flexural strength (a) and compressive strength (b) of Si_3N_4 porous ceramics.

solid content, which is clearly related to its porosity. As a result, the greatest strength (46.6 MPa) is gained from the sample with the lowest porosity. Generally, the higher the porosity, the weaker the mechanical strength, whereas a well-balanced pore structure can mitigate the reduction in strength or even increase it. The relationship between porosity and strength can be characterized as [31,32]:

$$\sigma = \sigma_0 \exp(-\beta P) \qquad (2)$$

where σ_0 is the flexural strength of the fully dense material, β is the structural factor (the smaller the value of β, the less sensitive the material is to porosity and the correspondingly higher strength is obtained), and P is the porosity. The relationship between the theoretical and experimental values of strength and porosity is demonstrated in Fig. S6 in the ESM.

Meanwhile, the fracture toughness curve of the Si_3N_4 porous ceramics is linearly related to the solid content, with the samples reaching a maximum fracture toughness of 6.71 MPa·m$^{1/2}$ at 25 vol% solid content. On one hand, the homogeneous pore size and evenly distributed interconnecting pores allow the cracks to branch and deflect in extension, facilitating high toughness in samples with high porosity. On the other hand, the interlacing of Si_3N_4 grains with high aspect ratios prolongs the path of crack expansion, and the internal spatial interlocking structure allows crack bridging and deflection to promote toughening [16,17]. At the same time, Fig. 12(b) and Fig. S7 in the ESM reveal that the porous Si_3N_4 ceramics have high compressive strength (up to 47.75 MPa), and the samples can maintain their integrity without obvious cracking and crushing after the compressive test.

Observation of the fracture surface indicates evidently in all samples that the elongated grains have undergone

penetration fracture, and the green arrows in Fig. 13 point out the fracture surface. The inset of Fig. 13(a) illustrates the tilted deflection of the crack at the grain interlap. Also, the pull-out phenomenon of the Si_3N_4 grains during bending was noticed. The yellow circle in Fig. 13 circles the dent left after grain pull-out and also remains the residue of low eutectic between grains (shown in insets of Figs. 13(a) and 13(b)). Therefore, porous Si_3N_4 ceramics with a high aspect ratio and homogeneous pore distribution can have good mechanical properties even with high porosity [17]. The mechanical strength for porous Si_3N_4 ceramics obtained in present work and in literature [8,9,12,14,33–46] as a function of porosity is presented in Fig. 14. It is apparent that the porous ceramics prepared by gelcasting–SHS have a considerable advantage in terms of porosity–strength. In summary, the process of gelcasting–SHS, which integrates the merits of both perfectly, is a potentially prospective method for the preparation of high-porosity (tunable porosity), high-strength porous Si_3N_4 ceramics.

4 Conclusions

We herein report the preparation of porous Si_3N_4 ceramics constituted by high aspect ratio grains and homogeneous pore distribution, via gelcasting–SHS process. The loose and porous internal space of the gel-casted green body facilitates favorable conditions for sufficient N_2 contact and the growth of long rod-like grains of β-Si_3N_4 during SHS. The porous Si_3N_4 ceramics with porosity of 67.83% to 78.03% are obtained, where the compressive strength reaches 11.79 to 47.75 MPa and fracture toughness reaches 1.20 to 6.71 MPa·m$^{1/2}$. The high-porosity and high-strength porous Si_3N_4 ceramics
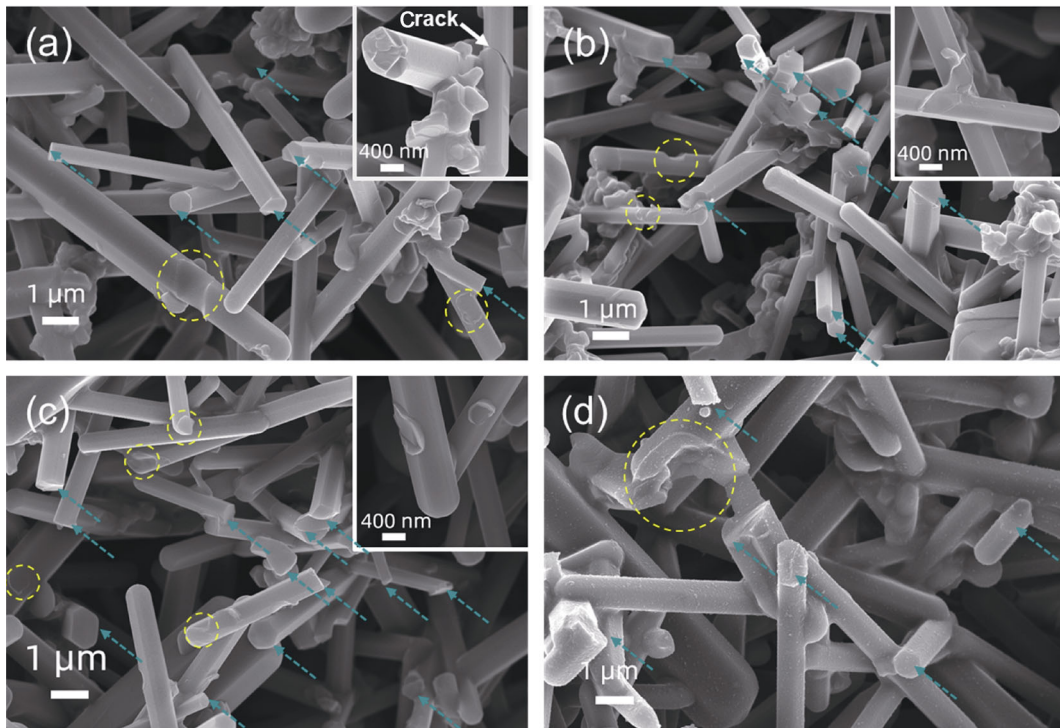
Fig. 13 Fracture surface morphology of the sample with different solid contents after flexural test: (a) 10 vol%, (b) 15 vol%, (c) 20 vol%, and (d) 25 vol%.
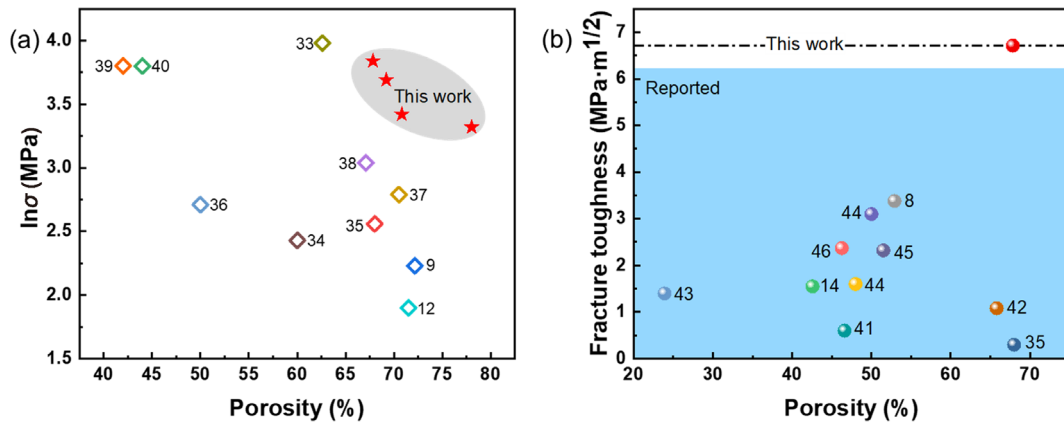
Fig. 14 (a) Comparison of flexural strength and (b) fracture toughness for porous Si_3N_4 ceramics obtained in present work and in literature as a function of porosity (numbers in the chart represent relevant references).

achieved by this simple and low-energy consumption method can potentially open opportunities in the fields of gas filtration, heat insulators, catalyst carriers, and wave-transparent which can offer new insights into the development of high-performance porous Si_3N_4 ceramics.

Acknowledgements

Electronic Supplementary Material

Supplementary material is available in the online version of this article at https://doi.org/10.1007/40145-021-0525-7.

References

[1]   Knickerbocker SH, Zangvil A, Brown SD. High-temperature mechanical properties and microstructures for hot-pressed silicon nitrides with amorphous and crystalline intergranular phases. *J Am Ceram Soc* 1985, **68**: C99–C101.

[2]   Cinibulk MK, Thomas G, Johnson SM. Strength and creep behavior of rare-earth disilicate–silicon nitride ceramics. *J*

Am Ceram Soc 1992, **75**: 2050–2055.

[3] Guo SQ, Hirosaki N, Nishimura T, *et al*. Hot-pressed silicon nitride with Lu$_2$O$_3$ additives: Oxidation and its effect on strength. *J Am Ceram Soc* 2003, **86**: 1900–1905.

[4] Yu J, Yang J, Li S, *et al*. Preparation of Si$_3$N$_4$ foam ceramics with nest-like cell structure by particle-stabilized foams. *J Am Ceram Soc* 2012, **95**: 1229–1233.

[5] Kalemtas A, Topates G, Özcoban H, *et al*. Mechanical characterization of highly porous β-Si$_3$N$_4$ ceramics fabricated via partial sintering & starch addition. *J Eur Ceram Soc* 2013, **33**: 1507–1515.

[6] Xia Y, Zeng YP, Jiang D. Mechanical and dielectric properties of porous Si$_3$N$_4$ ceramics using PMMA as pore former. *Ceram Int* 2011, **37**: 3775–3779.

[7] Cheng ZL, Ye F, Liu YS, *et al*. Mechanical and dielectric properties of porous and wave-transparent Si$_3$N$_4$–Si$_3$N$_4$ composite ceramics fabricated by 3D printing combined with chemical vapor infiltration. *J Adv Ceram* 2019, **8**: 399–407.

[8] Yin S, Pan LM, Huang K, *et al*. Porous Si$_3$N$_4$ ceramics with hierarchical pore structures prepared by gelcasting using DMAA as gelling agent and PS as pore-forming agent. *J Alloys Compd* 2019, **805**: 69–77.

[9] Hu YD, Zuo KH, Xia YF, *et al*. Microstructure and permeability of porous Si$_3$N$_4$ supports prepared via SHS. *Ceram Int* 2021, **47**: 1571–1577.

[10] Li XQ, Yao DX, Zuo KH, *et al*. Microstructure and gas permeation performance of porous silicon nitride ceramics with unidirectionally aligned channels. *J Am Ceram Soc* 2020, **103**: 6565–6574.

[11] Li L, Li QG, Hong J, *et al*. Effect of Si$_3$N$_4$ solid contents on mechanical and dielectric properties of porous Si$_3$N$_4$ ceramics through freeze-drying. *J Alloys Compd* 2018, **732**: 136–140.

[12] Yao D, Xia Y, Zeng YP, *et al*. Fabrication porous Si$_3$N$_4$ ceramics via starch consolidation-freeze drying process. *Mater Lett* 2012, **68**: 75–77.

[13] Parsi A, Golestani-Fard F, Mirkazemi SM. The effect of gelcasting parameters on microstructural optimization of porous Si$_3$N$_4$ ceramics. *Ceram Int* 2019, **45**: 9719–9725.

[14] Wu JM, Zhang XY, Yang JL. Novel porous Si$_3$N$_4$ ceramics prepared by aqueous gelcasting using Si$_3$N$_4$ poly-hollow microspheres as pore-forming agent. *J Eur Ceram Soc* 2014, **34**: 1089–1096.

[15] Zhang Y, Yao D, Zuo K, *et al*. Fabrication and mechanical properties of porous Si$_3$N$_4$ ceramics prepared via SHS. *Ceram Int* 2019, **45**: 14867–14872.

[16] Wang L, He G, Yang ZC, *et al*. Combustion synthesis of high flexural strength, low linear shrinkage and machinable porous β-Si$_3$N$_4$ ceramics. *J Eur Ceram Soc* 2021, **41**: 2395–2399.

[17] Zhang Y, Yao DX, Zuo KH, *et al*. Effects of N$_2$ pressure and Si particle size on mechanical properties of porous Si$_3$N$_4$ ceramics prepared via SHS. *J Eur Ceram Soc* 2020, **40**: 4454–4461.

[18] Zhang Y, Yu X, Gu H, *et al*. Microstructure evolution and high-temperature mechanical properties of porous Si$_3$N$_4$ ceramics prepared by SHS with a small amount of Y$_2$O$_3$ addition. *Ceram Int* 2021, **47**: 5656–5662.

[19] Su L, Li M, Wang H, *et al*. Resilient Si$_3$N$_4$ nanobelt aerogel as fire-resistant and electromagnetic wave-transparent thermal insulator. *ACS Appl Mater Interfaces* 2019, **11**: 15795–15803.

[20] Zhang X, Yuan J, Ding Y, *et al*. Directly growing nanowire-assembled nanofibrous ceramic foams with multi-lamellar structure via freeze-casting process. *J Eur Ceram Soc* 2021, **41**: 1041–1047.

[21] Chen R, Huang Y, Wang CA, *et al*. Ceramics with ultra-low density fabricated by gel casting: An unconventional view. *J Am Ceram Soc* 2007, **90**: 3424–3429.

[22] Hu LF, Wang CG, Huang Y. Porous yttria-stabilized zirconia ceramics with ultra-low thermal conductivity. *J Mater Sci* 2010, **45**: 3242–3246.

[23] Hu LF, Wang CG. Effect of sintering temperature on compressive strength of porous yttria-stabilized zirconia ceramics. *Ceram Int* 2010, **36**: 1697–1701.

[24] Chen D, Zhang B, Zhuang HR, *et al*. Combustion synthesis of network silicon nitride porous ceramics. *Ceram Int* 2003, **29**: 363–364.

[25] Cano IG, Rodríguez MA. Synthesis and sintering of Si$_3$N$_4$ obtained by the SHS process. *Ind Eng Chem Res* 2006, **45**: 1277–1280.

[26] Yao D, Xia Y, Zuo KH, *et al*. Porous Si$_3$N$_4$ ceramics prepared via partial nitridation and SHS. *J Eur Ceram Soc* 2013, **33**: 371–374.

[27] Chen Y, Zhang C, Wang N, *et al*. Synthesis and properties of self-assembled ultralong core–shell Si$_3$N$_4$/SiO$_2$ nanowires by catalyst-free technique. *Ceram Int* 2019, **45**: 20040–20045.

[28] Gao P, Xu J, Piao Y, *et al*. Deposition of silicon carbon nitride thin films by microwave ECR plasma enhanced unbalance magnetron sputtering. *Surf Coat Technol* 2007, **201**: 5298–5301.

[29] Han L, Wang JK, Li FL, *et al*. Low-temperature preparation of Si$_3$N$_4$ whiskers bonded/reinforced SiC porous ceramics via foam-gelcasting combined with catalytic nitridation. *J Eur Ceram Soc* 2018, **38**: 1210–1218.

[30] Li S, Wang CG, Yang F, *et al*. Hollow-grained "Voronoi foam" ceramics with high strength and thermal superinsulation up to 1400 ℃. *Mater Today* 2021, **46**: 35–43.

[31] Bergström L. Rheological properties of concentrated, nonaqueous silicon nitride suspensions. *J Am Ceram Soc* 1996, **79**: 3033–3040.

[32] Coble RL, Kingery WD. Effect of porosity on physical properties of sintered alumina. *J Am Ceram Soc* 2006, **39**: 377–385.

[33] Sun Y, Zhao Z, Li X, *et al*. A novel aerogels/porous Si$_3$N$_4$ ceramics composite with high strength and improved thermal insulation property. *Ceram Int* 2018, **44**: 5233–5237.

[34] Liu TT, Jiang C, Guo W. Effect of CeO$_2$ on low temperature pressureless sintering of porous Si$_3$N$_4$ ceramics. *J Rare Earths* 2017, **35**: 172–176.

[35] Li X, Zhang L, Yin X. Microstructure and mechanical properties of three porous Si₃N₄ ceramics fabricated by different techniques. *Mater Sci Eng*: A 2012, **549**: 43–49.

[36] Wang F, Gu H, Yin JW, *et al*. Porous Si₃N₄ ceramics fabricated through a modified incomplete gelcasting and freeze-drying method. *Ceram Int* 2017, **43**: 14678–14682.

[37] Hu HL, Zeng YP, Xia YF, *et al*. High-strength porous Si₃N₄ ceramics prepared by freeze casting and silicon powder nitridation process. *Mater Lett* 2014, **133**: 285–288.

[38] Xia Y, Zeng YP, Jiang D. Microstructure and mechanical properties of porous Si₃N₄ ceramics prepared by freeze-casting. *Mater Des* 2012, **33**: 98–103.

[39] Hu S, Li A, Feng B, *et al*. A non-sintering fabrication method for porous Si₃N₄ ceramics via sol hydrothermal process. *Ceram Int* 2018, **44**: 19699–19705.

[40] Xia Y, Zeng YP, Jiang D. Dielectric and mechanical properties of porous Si₃N₄ ceramics prepared via low temperature sintering. *Ceram Int* 2009, **35**: 1699–1703.

[41] Li X, Zhang L, Yin X. Fabrication and properties of porous Si₃N₄ ceramic with high porosity. *J Mater Sci Technol* 2012, **28**: 1151–1156.

[42] Yue J, Dong B, Wang H. Porous Si₃N₄ fabricated by phase separation method using benzoic acid as pore-forming agent. *J Am Ceram Soc* 2011, **94**: 1989–1991.

[43] Li X, Yin X, Zhang L, *et al*. Mechanical and dielectric properties of porous Si₃N₄–SiO₂ composite ceramics. *Mater Sci Eng*: A 2009, **500**: 63–69.

[44] Yang J, Yang JF, Shan SY, *et al*. Effect of sintering additives on microstructure and mechanical properties of porous silicon nitride ceramics. *J Am Ceram Soc* 2006, **89**: 3843–3845.

[45] Yin S, Pan LM, Fang X, *et al*. Porous Si₃N₄ ceramics prepared by aqueous gelcasting using low-toxicity DMAA system: Regulatable microstructure and properties by monomer content. *Ceram Int* 2019, **45**: 9994–10003.

[46] Li B, Jiang P, Yan MW, *et al*. Characterization and properties of rapid fabrication of network porous Si₃N₄ ceramics. *J Alloys Compd* 2017, **709**: 717–723.